



Jupiter's Mesoscale Waves Observed at $5\ \mu\text{m}$ by Ground-based Observations and *Juno* JIRAM

Leigh N. Fletcher¹, H. Melin¹, A. Adriani², A. A. Simon³, A. Sanchez-Lavega⁴, P. T. Donnelly¹, A. Antuñano¹, G. S. Orton⁵, R. Hueso⁴, E. Kraaikamp⁶, M. H. Wong⁷, M. Barnett⁷, M. L. Moriconi⁸, F. Altieri², and G. Sindoni²

¹Department of Physics and Astronomy, University of Leicester, University Road, Leicester, LE1 7RH, UK; leigh.fletcher@le.ac.uk

²INAF-Istituto di Astrofisica e Planetologia Spaziali, Roma, Italy

³NASA Goddard Space Flight Center Solar System Exploration Division (690) Greenbelt, MD 20771, USA

⁴Departamento de Física Aplicada I, Escuela de Ingeniería de Bilbao, UPV/EHU, Plaza Ingeniero Torres Quevedo, 1, E-48013 Bilbao, Spain

⁵Jet Propulsion Laboratory, California Institute of Technology, 4800 Oak Grove Drive, Pasadena, CA 91109, USA

⁶Jourdanstraat 121/8, B-1060, Sint-Gillis, Belgium

⁷University of California at Berkeley, Astronomy Department, Berkeley, CA 947200-3411, USA

⁸CNR-Istituto di Scienze dell'Atmosfera e del Clima, Bologna e Roma, Italy

Received 2018 April 30; revised 2018 June 13; accepted 2018 June 18; published 2018 July 26

Abstract

We characterize the origin and evolution of a mesoscale wave pattern in Jupiter's North Equatorial Belt (NEB), detected for the first time at $5\ \mu\text{m}$ using a 2016–17 campaign of “lucky imaging” from the VISIR instrument on the Very Large Telescope and the NIRI instrument on the Gemini observatory, coupled with M -band imaging from *Juno*'s JIRAM instrument during the first seven *Juno* orbits. The wave is compact, with a $1^\circ.1$ – $1^\circ.4$ longitude wavelength (wavelength 1300–1600 km, wavenumber 260–330) that is stable over time, with wave crests aligned largely north–south between 14°N and 17°N (planetographic). The waves were initially identified in small (10° longitude) packets immediately west of cyclones in the NEB at 16°N but extended to span wider longitude ranges over time. The waves exhibit a 7–10 K brightness temperature amplitude on top of an ~ 210 K background at $5\ \mu\text{m}$. The thermal structure of the NEB allows for both inertio-gravity waves and gravity waves. Despite detection at $5\ \mu\text{m}$, this does not necessarily imply a deep location for the waves, and an upper tropospheric aerosol layer near 400–800 mbar could feature a gravity wave pattern modulating the visible-light reflectivity and attenuating the $5\text{-}\mu\text{m}$ radiance originating from deeper levels. Strong rifling activity appears to obliterate the pattern, which can change on timescales of weeks. The NEB underwent a new expansion and contraction episode in 2016–17 with associated cyclone–anticyclone formation, which could explain why the mesoscale wave pattern was more vivid in 2017 than ever before.

Key words: planets and satellites: atmospheres – planets and satellites: gaseous planets – infrared: planetary systems

1. Introduction

Jupiter's $5\text{-}\mu\text{m}$ window is a unique region of the infrared spectrum where a dearth of gaseous opacity permits deep observations of Jupiter's cloud-forming region below the stably stratified upper troposphere (e.g., Terile & Westphal 1977). Although reflected sunlight from upper tropospheric clouds and hazes contributes in Jupiter's zones, the dominant contribution in the belts is from thermal emission in the 4–8 bar range, with clouds appearing in silhouette against the bright background of the warm troposphere. The window is bounded at long wavelengths by the $2\nu_2$ and ν_4 absorption bands of NH_3 and at short wavelengths by phosphine absorption in the broad $\nu_2 + \nu_4$ band between 4.69 and $4.78\ \mu\text{m}$. A host of additional disequilibrium species (AsH_3 , GeH_4 , CO, etc.) contribute to the spectrum, but these are all modulated by opacity variations in aerosol layers—both the upper tropospheric clouds related to NH_3 ice formation and the midtropospheric clouds associated with the formation of NH_4SH (Giles et al. 2015, 2017a). Water ice may also contribute opacity in certain regions (Bjoraker et al. 2015). Combined, this makes the $5\text{-}\mu\text{m}$ window useful as a diagnostic of the dynamics and circulation of the cloud-forming region.

Numerous studies have exploited this window in the past decade, ranging from space-based observations at low-spectral resolution by *Cassini* VIMS (Giles et al. 2015) and *Juno*

JIRAM (Grassi et al. 2017); to ground-based spectra at high spectral resolution by the Very Large Telescope (VLT; Giles et al. 2015, 2017a, 2017b), Gemini (Bjoraker et al. 2015), and the IRTF (Fletcher et al. 2016a); to narrowband photometric imaging from the IRTF, Gemini, and Keck. Thermal imaging has been used to explore the dynamics of the Great Red Spot (Fletcher et al. 2010), the bright peripheral rings around other vortices (de Pater et al. 2010), and the changes in aerosol opacity associated with Jupiter's belt/zone fades and revivals (Fletcher et al. 2011, 2017a). Observations at $5\ \mu\text{m}$ were therefore deemed to be an essential component of the Earth-based supporting campaign for NASA's *Juno* mission (Bolton et al. 2017), both preceding its arrival in 2016 July and during each of its 53.5 day polar orbits. In this work, we report on the use of a new capability of ESO's VLT Imager and Spectrometer for the mid-infrared (VISIR; Lagage et al. 2004), allowing it to perform “lucky imaging” of Jupiter in burst mode to “freeze” the seeing and provide diffraction-limited performance at $5\ \mu\text{m}$. This removes the need for adaptive optics using the Galilean satellites for wavefront sensing (de Pater et al. 2010), therefore increasing the flexibility of observations so that they could be designed to coincide with each of *Juno*'s perijoves. These are supplemented by *Juno* JIRAM M -band images with partial spatial coverage in 2016–17 and an additional campaign of M -band

lucky imaging with the Near InfraRed Imager and Spectrometer (NIRI) instrument on Gemini-North.

The VLT images provide nearly full-disk coverage of Jupiter at spatial resolutions of $0''.15$, equating to horizontal resolutions of ~ 470 km at opposition ($0^\circ 39'$ longitude at the equator) and ~ 570 km at quadrature ($0^\circ 46'$ longitude). At this resolution, it is possible to resolve structures less than a degree of longitude in width, providing $5\text{-}\mu\text{m}$ access to length scales typical of the *Hubble Space Telescope* (Simon et al. 2018) and the best amateur imagers. In particular, we reach the ~ 1400 km length scale of a wave pattern in Jupiter’s North Equatorial Belt (NEB) near 16°N (planetographic latitude) that was previously reported by *Voyager 2* (Smith et al. 1979) and later rediscovered in *Hubble* imaging in 2015 January (Simon et al. 2015). Simon et al. (2015) suggested that these “mesoscale” waves were formed via a baroclinic instability mechanism potentially associated with cyclogenesis, but the rarity of their presence proved a challenge to more detailed analysis. The VLT $5\text{-}\mu\text{m}$ imaging coincided with their dramatic reappearance in 2016–17, at a time when the NEB was undergoing an expansion and contraction episode as part of its 4–5 yr cycle (Fletcher et al. 2017b). In two companion articles, Simon et al. (2018) reported the properties of the NEB wave as observed in the visible range by *Hubble* and amateur ground-based imaging, and A. Adriani et al. (2018, in preparation) reported on *Juno* spectroscopy of the wave pattern. Section 2 describes the lucky-imaging process used to acquire the VLT data and reveals that this wave is detectable at $5\text{-}\mu\text{m}$, Section 3 describes the chronology of the mesoscale wave pattern and its association with NEB activity, and Section 4 explores the implications of the $5\text{-}\mu\text{m}$ detection and the different potential wave mechanisms responsible for this pattern.

2. Data Acquisition

2.1. VISIR Observations

VISIR (Lagage et al. 2004) returned to the 8.2 m UT3/Melipal telescope in 2015 after a 3 yr refurbishment. The new 1024×1024 Raytheon Aquarius IBC detector offers a pixel size of $0''.0453 \text{ pixel}^{-1}$ over a $38'' \times 38''$ field of view, smaller than the disk of Jupiter at opposition but sufficient to oversample the $0''.15$ spatial resolution of the $5\text{-}\mu\text{m}$ imaging. Following interactions with Hans-Ulrich Kaufl in 2015 March, an *M*-band filter was located and inserted into VISIR. Given the high sky background, the individual integration times are usually a few milliseconds, and the upgraded VISIR now offers a new burst mode whereby all individual detector exposures are recorded, rather than just retaining the averages per nodding cycle. We were awarded Science Verification observations in Period 96 (2016 February), immediately prior to *Juno*’s arrival at Jupiter, to test this new *M*-band “lucky-imaging” capability. Once validated, this became a part of our regular observing sequence in Period 98 (2016 December onward). We targeted all opportunities when Jupiter was available for more than 1 hr within a week of *Juno*’s perijove encounters. Unfortunately, weather constraints at Paranal and scheduling competition for service-mode observations restricted the data set to six distinct epochs, as shown in Table 1. The epochs were primarily clustered during the 2016–17 apparition (centered on Jupiter’s opposition on 2017 April 07). Regular observations at $7\text{--}20\text{-}\mu\text{m}$ (i.e., without burst mode) demonstrated the changes associated

with the NEB expansion during this period (Fletcher et al. 2017b).

A single observing block has N_{nod} nodding cycles (usually four or five), each producing two files: the first performed chopping on Jupiter itself, the second performed chopping at a position $25''$ away. The observations were designed such that the direction of the chop was determined by the particular hemisphere that we were focusing on: chopping the telescope north if we desired unobstructed views of the northern hemisphere, and chopping the telescope south if we wanted unobstructed views of the southern hemisphere. The total integration time divided by the number of nodding cycles and the 3–4 Hz chopping frequency determined the number of chopping cycles within each individual file. The individual integration time of each frame was 11.4–20.8 ms, depending on the chopping frequency used. We took the sum of the chop-nod position that encompassed only blank sky and subtracted this from every frame of the chop-nod position that targeted Jupiter alone (effectively discarding 50% of the data). This produced hundreds of individual frames for each nodding cycle. These were saved as both MP4 files for quick inspection and uncompressed TIFF files for further processing. The movies show Jupiter moving around on the detector and coming in and out of focus as the seeing varies over millisecond timescales.

The TIFF files were imported into AutoStakkert,⁹ a software tool developed by E. Kraaikamp to identify and stack those frames with the best image quality (Kraaikamp 2016). The software centers and aligns the individual frames using a “surface” mode to track individual bright features within an alignment box on Jupiter throughout the sequence. The frame quality is estimated via measurements of local gradients from frame to frame and used to rank the frames from best to worst. One large alignment point, encompassing the NEB and South Equatorial Belt (SEB) of Jupiter, was then used as the anchor to stack the top 2%, 5%, 10%, and 20% of frames. As more frames sometimes worsened the quality of the stack, we made a qualitative selection of one stack for continued analysis. The limb of the planet was fitted to assign latitudes, longitudes, and emission angles to each pixel, which were then projected onto a $0''.25$ resolution cylindrical map. No attempt was made to radiometrically calibrate the data.

2.2. Gemini Observations

The VISIR data were supplemented by a single mosaic $5\text{-}\mu\text{m}$ image from NIRI (Hodapp et al. 2003) on Gemini-North using a similar lucky-imaging process without adaptive optics. NIRI’s 1024×1024 pixel InSb array and $0''.0218 \text{ pixel}^{-1}$ scale limits the field of view to $22 \times 22''$, which was mosaicked across the disk to generate a map on 2017 February 5 (Table 1). Details of the wider Gemini/NIRI program will be described in a forthcoming paper.

2.3. Juno JIRAM Observations

The ground-based observations are compared to partial maps of the NEB acquired by the JIRAM instrument on the *Juno* spacecraft. The JIRAM imager and spectrometer (Adriani et al. 2017) are mounted on the *Juno* spacecraft and have been operating since 2016 August. *Juno* approaches the planet every 53 days with different attitudes according to primary science

⁹ autostakkert.com

Table 1
Observations at 5 μm Presented in This Work

Date	Observations	Number of Obs.	ID	Comments
2016 Feb 26	05:48–06:20	4	60.A-9620	Science verification, no waves 30°W–160°W
2016 Aug 27	JIRAM PJ1	Waves 36°W–52°W
2016 Dec 18	08:21–08:25	1	098.C-0681	Waves 80°W–105°W
2017 Jan 11	08:29–08:33	1	098.C-0681	Waves 95°W–117°W
2017 Feb 02	JIRAM PJ4	Waves 68°W–82°W
2017 Feb 05	14:13–15:48	62	GN-2017A-Q-60	Waves 44°W–70°W + 165°W–193°W
2017 Feb 06	05:45–05:49	1	098.C-0681	No waves 230°W–360°W
2017 Mar 16	05:41–05:46	1	098.C-0681	No waves 200°W–320°W
2017 Mar 27	JIRAM PJ5	Waves 40°W–85°W
2017 May 19	JIRAM PJ6	No waves 205°W–260°W
2017 Jul 11	JIRAM PJ7	Waves 280°W–30°W
2017 Jul 20	01:04–01:17	1	099.C-0612	No waves 280°W–50°W (poor seeing)

Note. The system III longitudes span from east to west.

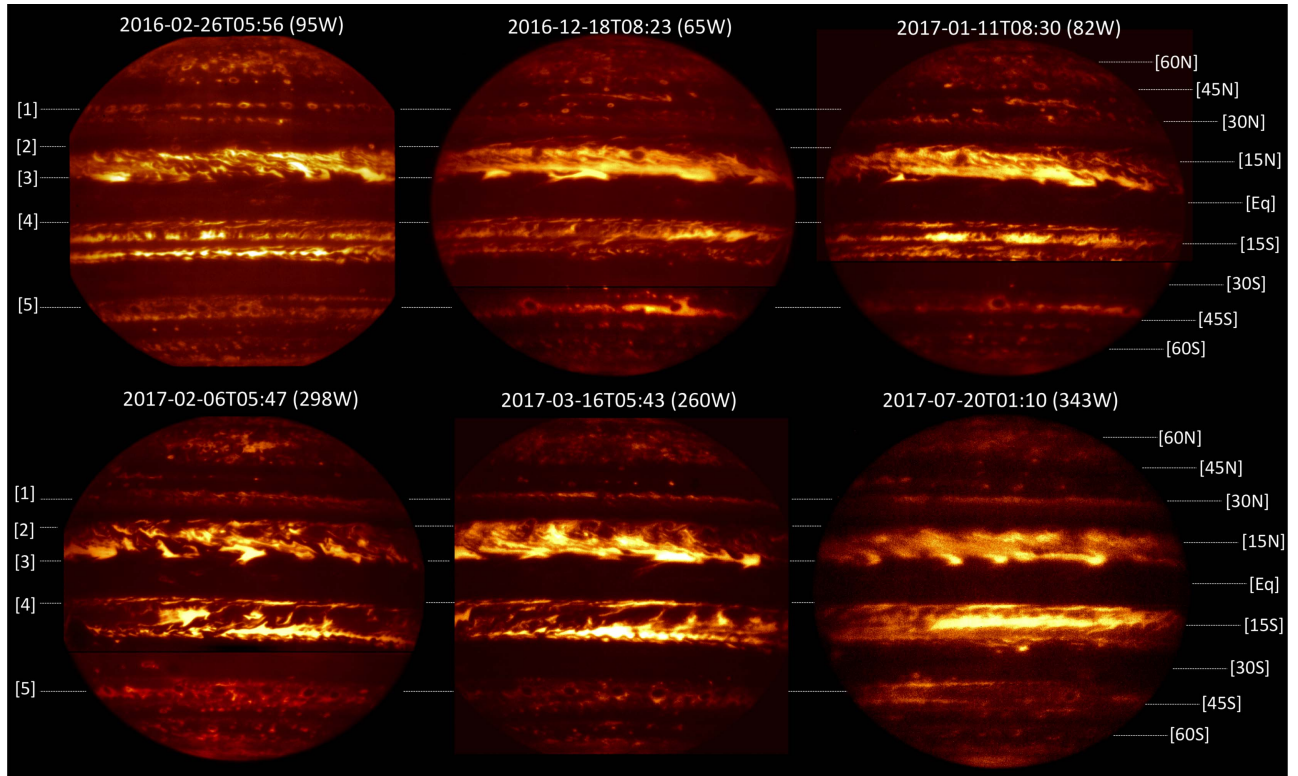


Figure 1. Six examples of VISIR burst-mode imaging at 5 μm . The 2016 December, 2017 January, and 2017 February images were assembled from two sets of images, one targeting the north and one targeting the south. Horizontal numbered lines indicate regions discussed in the main text and [Appendix](#), and a latitude scale is included on the right-hand side. The central meridian longitude is indicated in each frame.

objectives (Bolton et al. 2017). In the first part of the mission, most of the flybys were favorable to JIRAM, and the planet could be observed during the approach with good views of the northern hemisphere. The NEB was observed with variable coverage during orbits 1, 4, 5, 6, and 7 (during orbits 2 and 3, the instrument was not operating). The JIRAM imager has a channel working around 5- μm wavelength. Single images have a size of 432×128 pixels. Pixels are square-shaped with an angular resolution of $240 \times 240 \mu\text{m}$, which defines the spatial resolution at the cloud level as a function of the distance of the spacecraft from the planet. The images reported hereafter present an average spatial resolution of about 250 km at the cloud level, twice as good as the VLT resolution reported above. When the spacecraft’s spinning plane intersects the

planet, JIRAM can make scans from south to north, changing pointing approximately every 30 s (spacecraft spinning period). Maps of a limited range of latitudes can be built by mosaicking images from different observing sequences, although some artifacts occur because the atmosphere has evolved during the interval between sequences. Dates of the JIRAM data acquisitions are reported in Table 1.

3. Results

Figure 1 presents the full-disk images of Jupiter acquired using VISIR’s burst mode between 2016 and 2017, providing global context for the NEB activity. Figure 2 provides a larger-scale example of a northern hemisphere image in 2017 January, with the NEB wave pattern highlighted. This was the first

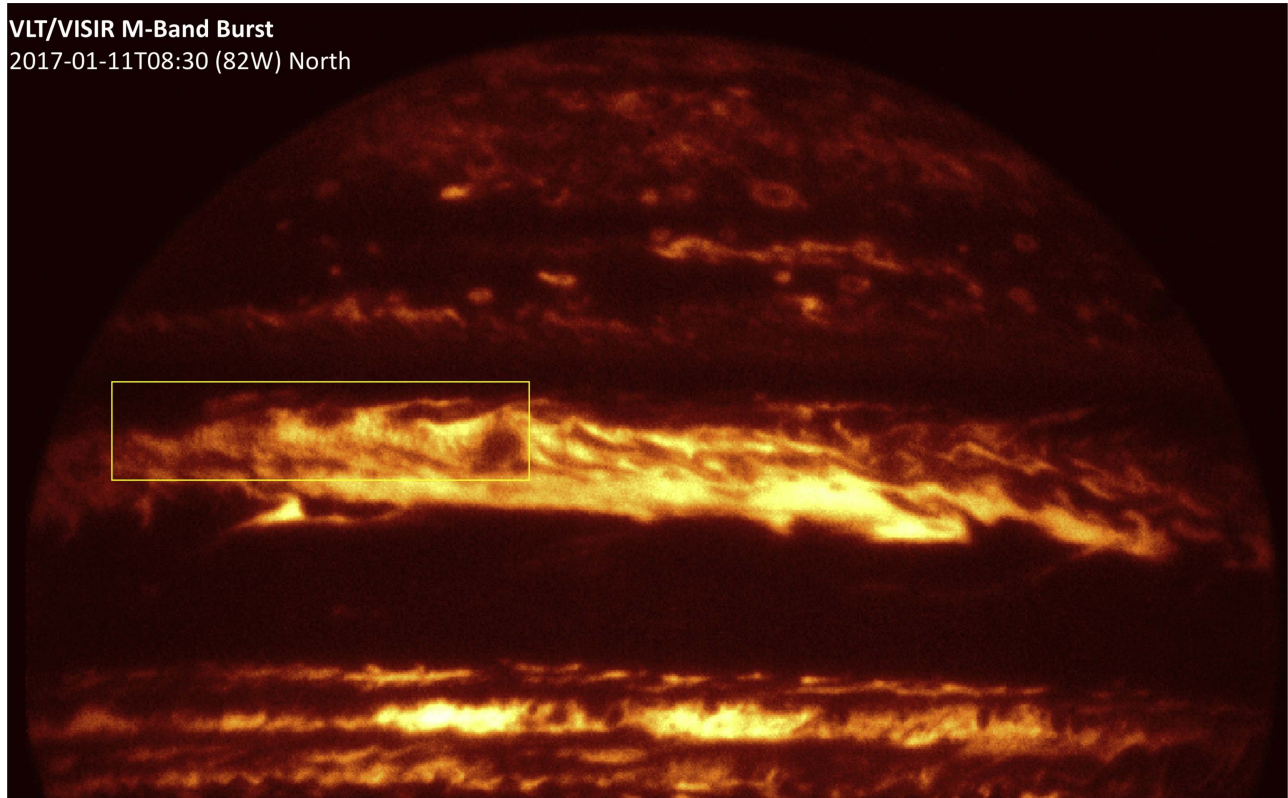


Figure 2. Close-up view of the VLT 5- μ m observations in 2017 January, highlighting the mesoscale waves to the west of the dark cyclone B1.

evidence that the NEB wave of Simon et al. (2015) was visible at 5 μ m and supported the view that it could be associated with cyclogenesis.

3.1. Status of the NEB in 2016–17

Figure 3 shows the evolution of the NEB during a new phase of NEB expansion in 2017 (all latitudes are planetographic). During these expansion events, the dark coloration of the NEB is seen to extend from 17°N to 20°N, encroaching on the typically white North Tropical Zone (NTrZ; region [2] of Figure 1). This dark coloration coincides with warmer temperatures and bright 5- μ m emission, implying the removal of the white NTrZ aerosols during an expansion. The first phase of the expansion in 2015–16 was documented by Fletcher et al. (2017b) but had stalled and regressed by the time of *Juno*’s arrival in 2016 July and never spanned all longitudes. At its peak, the expanded region spanned $\sim 145^\circ$ of longitude west of a large anticyclone (White Oval Z; 19°N, 283°W in 2016 February). The expanded region reached an unusual cyclone–anticyclone pair, which was observed during our first VLT lucky-imaging campaign in 2016 February (Figure 4), before *Juno*’s arrival. The anticlockwise motion of the cyclone can be observed near 16°N, 55°W, embedded within the NEB. This cyclone will be labeled B1 for the purposes of this study. The anticlockwise motion of the anticyclone can be seen at 19°N, 43°W, nominally within the NTrZ. The expanded NEB had regressed at all longitudes by the time of *Juno*’s arrival, and the NEB had its normal width in 2016 August (Figure 5(a)) and 2016 December (Figure 3).

Maps in 2017 February and March (Figure 3) show a second phase of cloud clearing within the NTrZ, where the 5- μ m emission is visible at latitudes poleward of the NEBn jet at 17°

N (planetographic). This time, the expansion spread over all longitudes. At the end of an expansion episode, the undulations of the northern edge of the NEB transform into a chain of cyclones near 16°N (sometimes known as barges) and anticyclonic white ovals (AWOs) near 19°N (Fletcher et al. 2017b; Rogers 2017). This pattern of cyclone–anticyclone pairs can be seen in 2017 March (see Section 3.2). In addition, the southern edge of the NEB (region [3] in Figure 1) exhibits the familiar chain of 5- μ m bright hot spots that move rapidly eastward with the prograde NEBs jet at 7°N. The influence of the NEB expansion and the presence of the NEB cyclones will be described in Section 3.2.

3.2. Chronology of NEB Waves

In this section, we present the chronology of the NEB wave activity as observed at 5 μ m. The prerequisite for observing the waves at this wavelength is the presence of a relatively quiescent background 5- μ m emission that can be modulated solely by the waves, rather than other phenomena, like vortices, convective plumes, and “rifts,” which appear dark and cloudy against the bright background emission. For ground-based observers, these conditions were met in 2016 December and 2017 January–February (Figure 6), when the mesoscale waves were first identified at 5 μ m. The 2016 February 5- μ m observations (Figure 4) did not show the presence of waves, whereas the first JIRAM map (2016 August, Figure 5(a)) reveals hints of the wave pattern over a limited 12° longitude range to the west of a dark cyclone at 35°W, and these were clearly visible by the end of 2016 from the ground.

Timeline of the NEB cyclones.—Given the potential importance of cyclogenesis in the origins of the wave pattern (Simon et al. 2015), we now discuss their chronology in detail.

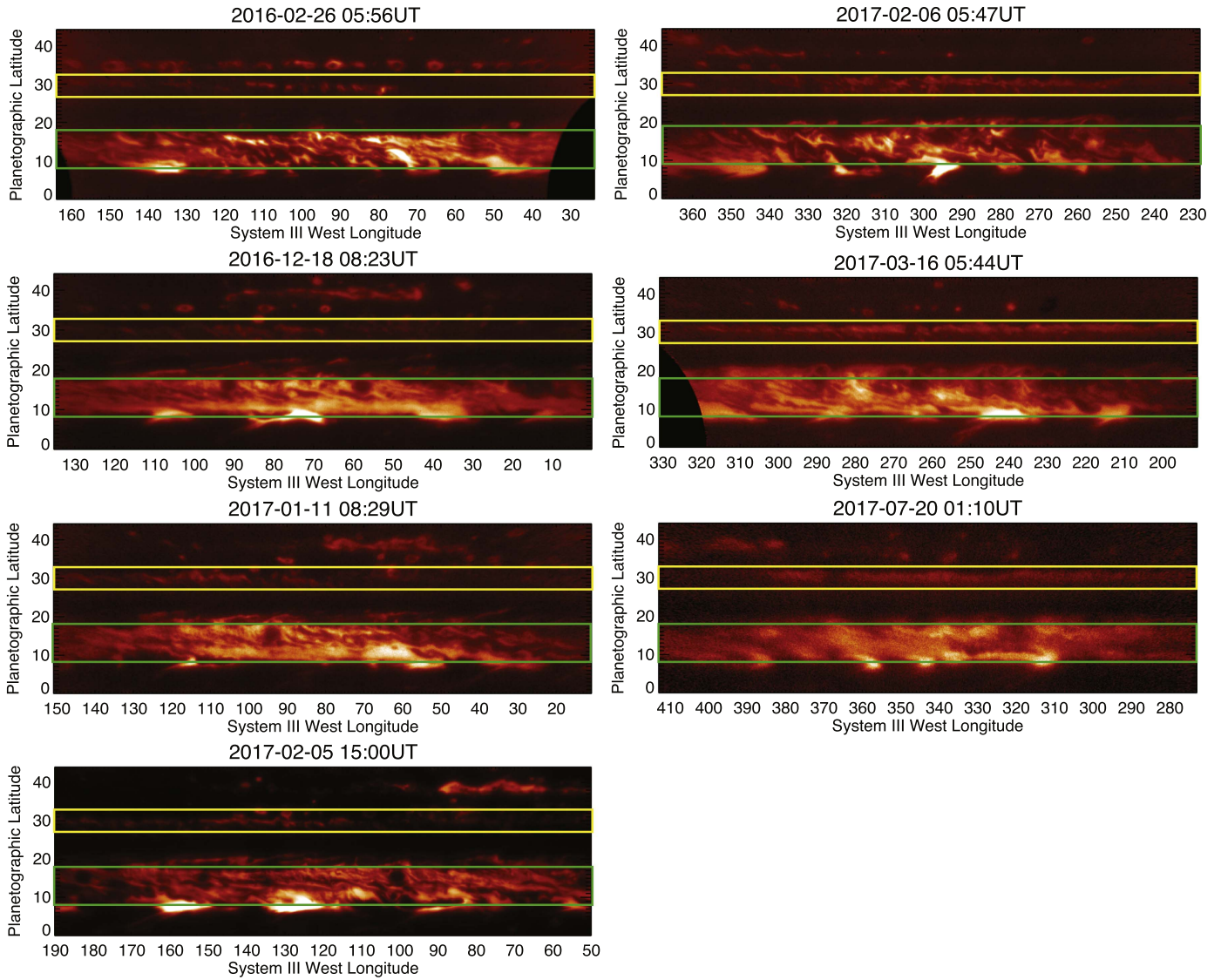


Figure 3. Maps of 5- μ m emission in the northern hemisphere, highlighting the NTB region in yellow and the NEB region in green.

In the August and December images, the waves appear to be located to the west of two cyclones. Figure 6 shows that the cyclone B1 moved 4° westward (from 90° W to 94° W) over 30 days between the December and January observations (0.13 day^{-1}). This slow motion is consistent with the weak winds in the center of the NEB. Extrapolating backward, this same cyclone B1 is observed at 75° W in 2016 August (Figure 5(a)) and 55° W in 2016 February (Figure 4). Indeed, B1 is the same cyclone that marked the westward extension of the stalled 2015–16 expansion and had been apparent in ground-based data since at least 2015 October (Fletcher et al. 2017b). This cyclone showed no wave pattern in 2016 August, but one had developed by 2016 December, 4 months later. The longevity of cyclone B1, which existed long before waves were identified, suggests that the waves may not originate from cyclone formation but rather from processes at work once the cyclone was already mature. Cyclone B1 was last definitively observed at 106° W in 2017 March (Figure 5(c)), at which time its wave train was no longer visible (it is visible in 2017 February in Gemini/NIRI observations; Figure 6). The second cyclone, B2 (35° W in 2016 August), formed within the previously expanded sector of the NEB and was the first to exhibit the

wave train in the *Juno* observations at 35° W. It was observed again near 58° W in 2016 December, this time without visible waves, but B2 is not visible in either the January VISIR maps or the 2017 February Gemini/NIRI maps (Figure 3), suggesting that the cyclone had dissipated.

Early views of the waves.—Observations between 2016 August (JIRAM), 2016 December, and 2017 January (VLT) suggest that the waves occurred in longitudinally confined packets. The NEB had its regular width (7° N– 17° N) at this stage, before the onset of the new 2017 expansion event. On 2016 August 27, the waves extended some 12° west of cyclone B2, but these had vanished by 2016 December when B2 was at 58° W, indicating a lifetime shorter than 4 months. Conversely, the December data showed a longitudinally confined wave train between 80° W and 105° W that had not been present in August. *Hubble* imaging on December 11 (Figure 6) also reported the wave between 70° W and 100° W (Simon et al. 2018). The waves appeared to exist within two 10° longitude wide packets on either side of cyclone B1 at 92° W that were latitudinally wider to the east ($\sim 3^\circ$) than to the west ($\sim 1^\circ$). This tapering could be related to a dark striation 1° further south in Figure 6, which extended from the southeast to the northwest. The

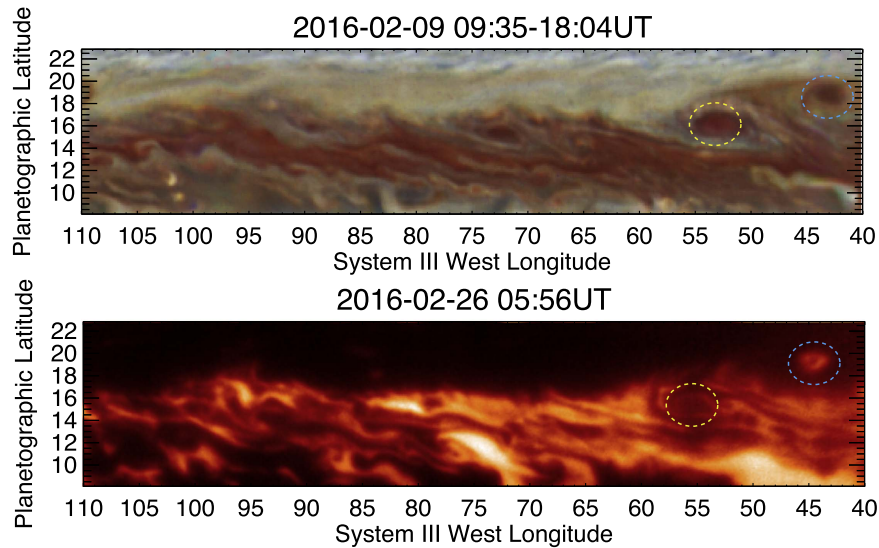


Figure 4. The 2016 February 26 observation of the NEB in a nonexpanded domain (Fletcher et al. 2017b) compared to *Hubble* imaging from the OPAL program on 2016 February 9 (17 days earlier). Cyclones equatorward of the NEBn jet are indicated by yellow ovals, and anticyclones poleward of the NEBn jet are indicated by blue ovals. Both *HST* and VLT images have been sharpened by means of a high-pass filter. No waves are detectable in this region. The cyclone B1 near 50°W–55°W shows an interior spiral pattern and existed immediately next to an anticyclone near 45°W. This cyclone–anticyclone pair had been present since at least 2015 October (Fletcher et al. 2017b) and marked the westward edge of the NEB expansion region.

wavelength was 1.3° in the January image and exhibited a slight tilt from southeast to northwest. The cyclone B1 and wave pattern moved $\sim 2^\circ$ westward (to 94° W) by January 11. The waves retained their 1.2 – 1.4° wavelength and northwesterly tilt and extended from 95° W to 117° W longitude. The latitudinal extent remained $\sim 2^\circ$ across the wave train. Once again, there is a qualitative suggestion that they existed in two distinct packets of approximately 10° longitude, although this could be a property of the underlying background emission rather than of the wave itself. JIRAM observations on 2017 February 2 (PJ4) only caught a small glimpse of the waves between 68° W and 82° W, extending over $\sim 14^\circ$ longitude (Figure 5(b)), and they were also detectable in Gemini/NIRI observations on February 5. There is a considerable amount of small structure at the same spatial scale that could support the presence of a more extensive wave pattern, as suggested by *Hubble* imaging on February 1, which reports waves from 25° W to 75° W (Simon et al. 2018).

Mature wave pattern.—In 2017 February–March, the NEB had expanded northward to 21° N (Figures 3 and 7), and a cyclone–anticyclone pattern formed from the “bulges” on the northern edge of the NEB that characterize expansion phases¹⁰ (Fletcher et al. 2017b). The February images reveal dark cyclones every $\sim 22^\circ$ of longitude in the 250° – 340° range at 16° N (Figure 7). By March, these had been joined by anticyclones near 20° N, with the anticyclones generally occurring to the northwest of the cyclones, although this pairing was not always consistent. The presence of this cyclone–anticyclone pattern caused the surrounding NEB to become turbulent and chaotic. With these features strongly modulating the background $5\text{-}\mu\text{m}$ flux, it proved impossible to observe the mesoscale waves in the 220° W– 320° W longitude range sampled by the VLT data.

So was the fine-scale (1.2° wavelength) wave pattern truly absent when the cyclone–anticyclone wave pattern (22° – 24° wavelength) developed, or is this just a consequence of the visibility at $5\text{-}\mu\text{m}$? *Hubble* imaging on February 1 and Gemini/NIRI imaging on February 5 showed waves in a relatively quiescent sector of the NEB over 160° W– 200° W (Figure 7, top) but not over the more complex 250° W– 320° W domain sampled by the VLT on February 6 (Figure 7, middle). This is consistent with turbulent activity removing all signatures of the waves. Further *Hubble* imaging on April 3 showed waves at (a) 5° W– 55° W and (b) 235° W– 305° W (Figure 7, bottom). The former are readily visible in the March 27 JIRAM observations (Figure 5(c)) spanning 45° W– 85° W. But the latter were not visible in the VLT images 18 days earlier (Figure 7). This suggests that the waves can still be present but not visible at $5\text{-}\mu\text{m}$ due to strong variation in the underlying emission. The *Hubble* observations in 2017 April (Simon et al. 2018) show a large-scale NEB rifting event (turbulent white cloud structures, sheared east near the NEBs and west near the NEBn) that spanned from 90° W to 220° W during this period, and it is notable that the waves are only visible outside of this longitude range.

Hubble imaging and amateur observations (Simon et al. 2018), as well as *Juno* observations from PJ7 (Figure 5(e)), suggest that the NEB wave was present away from the prominent rifting zone until at least 2017 July. Waves were not visible in the 260° W– 305° W range sampled by JIRAM during PJ6 but were visible 7–8 weeks later, spanning from 280° W to 30° W, confirming that they can develop and disappear over monthly timescales. We can conclude that the mesoscale waves form only in a relatively quiescent NEB, away from prominent rifts, and initially in association with preexisting cyclones.

¹⁰ We note that the cyclone–anticyclone pattern has the same 22° – 24° wavelength as the strong upper tropospheric thermal wave that was present in 2016 and anticorrelated with reflectivity from the upper tropospheric hazes (Fletcher et al. 2017b).

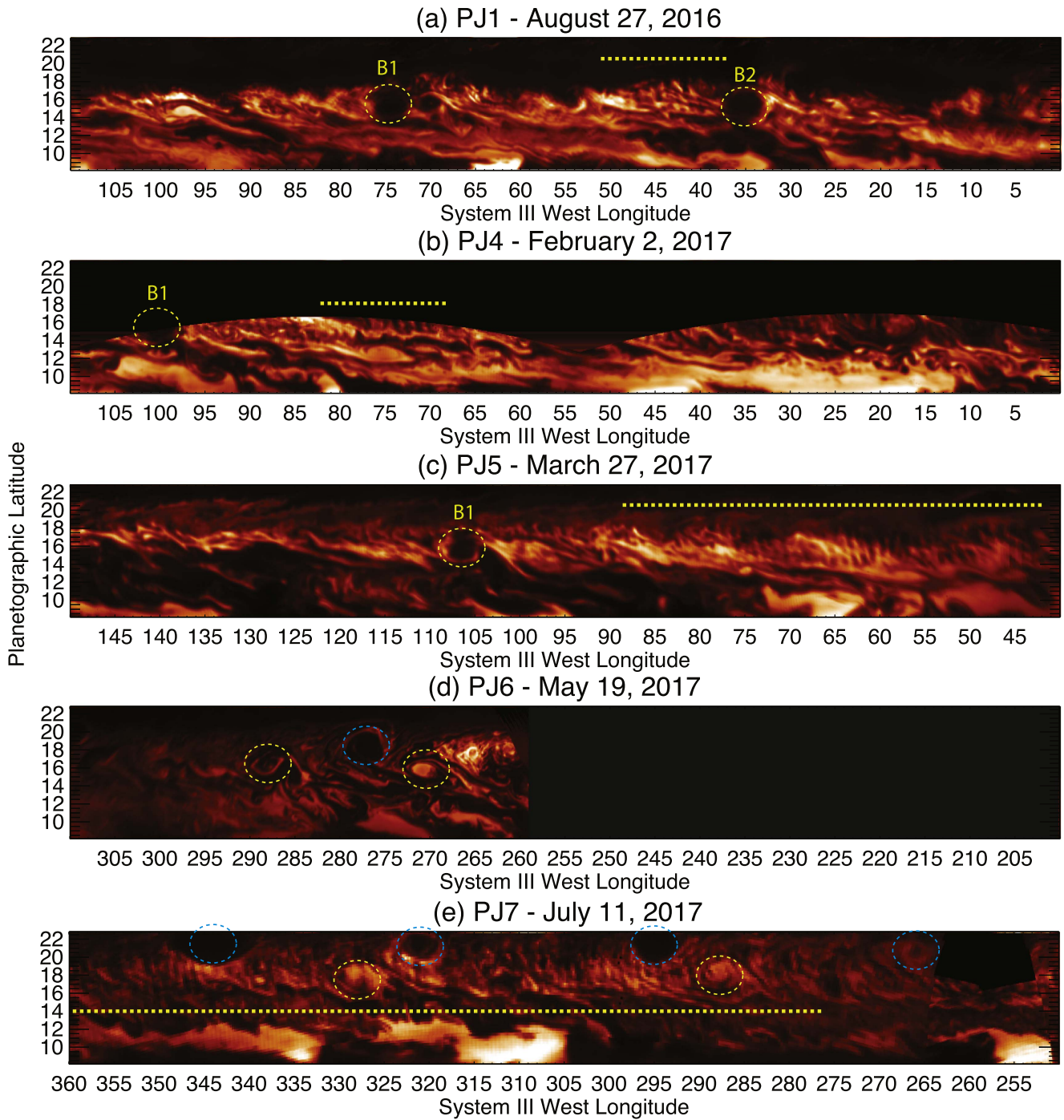


Figure 5. Cylindrical projections of *Juno* JIRAM 5- μ m data from PJ1 to PJ7 (excluding PJ2–3 when JIRAM was not on). Prominent cyclones are indicated by yellow ovals (B1 and B2 are labeled), and prominent anticyclones are indicated by blue ovals. The longitude range of potential mesoscale wave activity is shown by the yellow dotted line and is most clear during PJ5 (2017 March) and PJ7 (2017 July) data.

4. Discussion

4.1. Detection at 5 μ m

The primary conclusion of this work is that the mesoscale wave activity observed at visible wavelengths (Simon et al. 2015, 2018) also serves to modulate the 5- μ m emission from Jupiter’s deeper troposphere. This provides a new window for tracking this unusual phenomenon. However, the detection alone need not necessarily imply that the wave pattern is deep. First, there is a nonnegligible contribution from reflected sunlight at 5 μ m, which reflects off of the same

tropospheric clouds that are evident in the visible-light imaging (Bjoraker et al. 2015). A modulation of the upper tropospheric clouds could therefore influence the reflected sunlight contribution, but aerosols within the belts are expected to have a low albedo at 5 μ m. However, the upper tropospheric aerosols can modulate the 5- μ m radiance in the absence of reflected sunlight simply via absorption and scattering. Giles et al. (2015) required a cloud at $p < 1.2$ bar to reproduce *Cassini* VIMS spectra of both cloudy zones and cloud-free belts. Lower pressures were also permitted by the data, implying that this cloud could reside at the NH_3 condensation level near 800

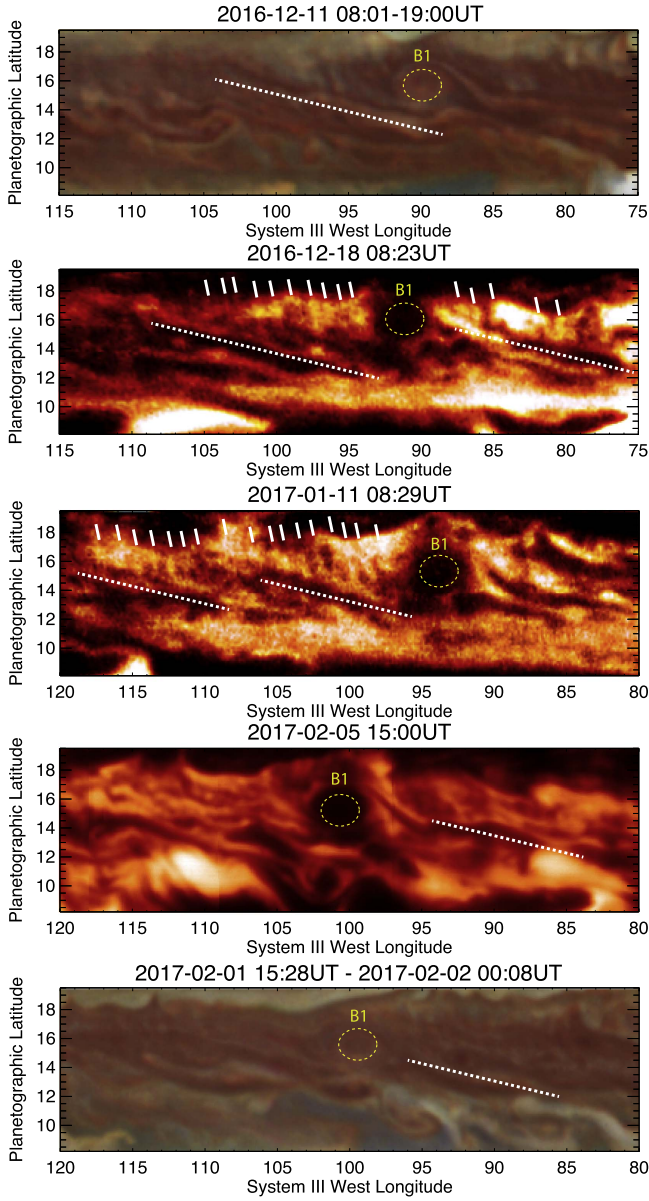


Figure 6. Observations of the mesoscale waves over a short longitude segment in 2016 December and 2017 February compared to *Hubble Space Telescope* observations on 2016 December 11 and 2017 February 1 (GO-14661). The NEB was not expanded at this time. Wave peaks are indicated by solid white lines, cyclone B1 is indicated by a yellow dotted oval, and the bright cloud streak (dark at $5\ \mu\text{m}$) is indicated by the diagonal white dotted line. Both *HST* and $5\text{-}\mu\text{m}$ images have been sharpened by means of a high-pass filter. Gemini/NIRI and *HST* observations in early February show that the wave pattern that had been present in January was no longer visible near B1.

mbar. Furthermore, Galileo NIMS analyses by Irwin et al. (2001), Nixon et al. (2001), and Irwin & Dyudina (2002) place the primary cloud decks in the 1–2 bar range, and Sromovsky & Fry (2010) suggested a spatially variable cloud base between 0.79 and 1.27 bar. Although optical thickness variations of a deeper cloud were also required to fit the $5\text{-}\mu\text{m}$ spectra, we have no way to determine whether the mesoscale wave modulation exists in the upper layer, the deeper layer, or both.

Each of these works are consistent with a possible source of $5\text{-}\mu\text{m}$ modulation in the 0.8–1.2 bar range without having to assume that the mesoscale wave is present at higher pressures. Near-infrared spectroscopy of the NEB is required to better constrain the altitude of the wave pattern, as described by A.

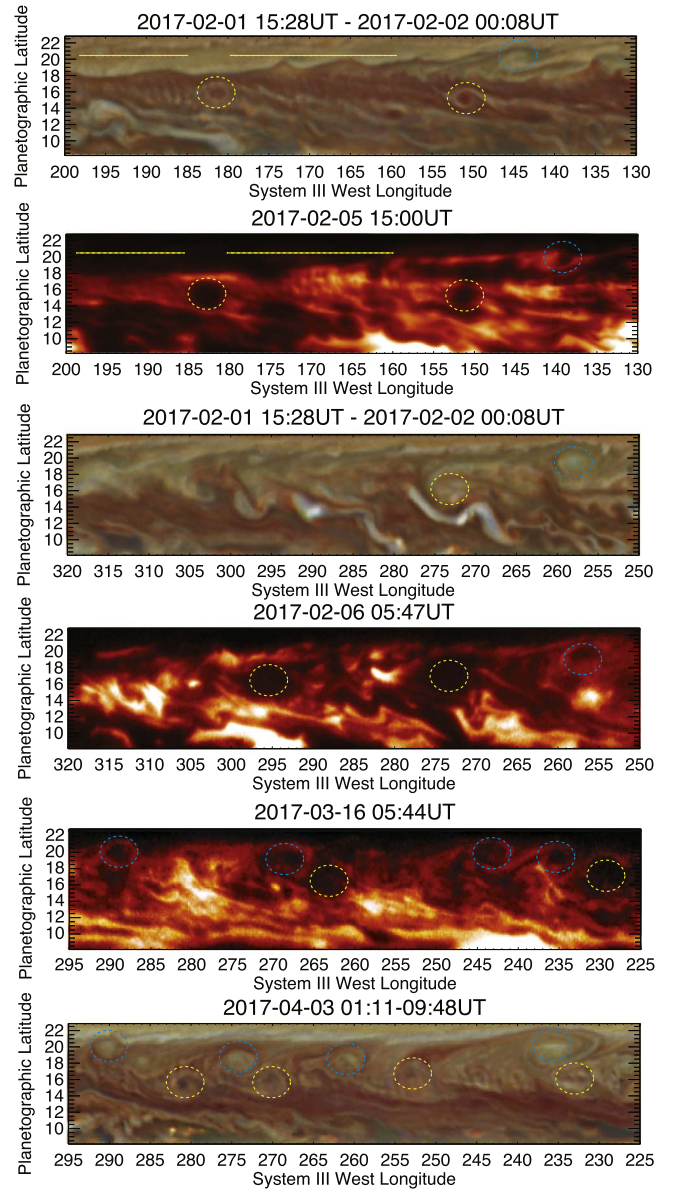


Figure 7. The VLT and Gemini observations obtained in 2017 February and March, once the cyclone–anticyclone pattern was forming. Waves were still visible in early February at more quiescent longitudes (horizontal yellow line in top panels) but were harder to distinguish at $5\ \mu\text{m}$ near locations of strong rifting (middle panels) of closely packed cyclones (yellow ovals) and anticyclones (blue ovals) in the bottom panels. However, this did not mean that they were absent, as clearly indicated in the *HST* imaging on 2017 April 3 (GO-14756). *Hubble* imaging from 2017 February 1 comes from GO-14661. Both *HST* and VLT images have been sharpened by means of a high-pass filter.

Adriani et al. (2018, in preparation) using JIRAM data. Their analysis also suggests that the data can be explained by waves in the upper layer, the deeper layer, or a combination of both. Although we cannot distinguish these possibilities, we favor a lower pressure for the reasons outlined above.

Finally, the calibrated *Juno* JIRAM data sets allow us to provide a quantitative estimate of the brightness amplitude of the wave pattern. The 2017 May observations (PJ5) have a mean brightness temperature at 16°N of $210 \pm 15\ \text{K}$, where the large range is a result of the extreme variability seen in Figure 5(c). The wave amplitude is 7–10 K peak to peak (approximately $2\ \mu\text{W cm}^{-2}\ \text{sr}^{-1}\ \mu\text{m}^{-1}$), where we caution the reader that this is a brightness temperature resulting from

aerosol modulation, rather than a physical temperature variation. The cyclone near 106°W reaches brightness temperatures of ~ 195 K, compared to a background of ~ 220 K. We find the same range of brightness temperatures in the PJ7 data. Via an analysis of *Cassini* VIMS spectra, Giles et al. (2015) demonstrated that changes of $2 \mu\text{W cm}^{-2} \text{sr}^{-1} \mu\text{m}^{-1}$ could easily be reproduced by changes in the opacity of a $p = 0.8$ bar cloud of 10%–20%, which suggests that upper tropospheric modulation of the deeper 5- μm radiance is a reasonable hypothesis.

4.2. Wave Origins and Nature

The chronology of the NEB wave described above raises several intriguing possibilities, which we summarize here.

1. Mesoscale waves were first observed at 5 μm in mid-2016 in association with two cyclones, B1 and B2, that were related to the stalled 2015–16 expansion of the NEB. Cyclone B1 had been present since at least 2015 October and had been part of a cyclone–anticyclone pair that marked the western edge of the expanded NEB sector. Given the rarity of the mesoscale waves and their redetection during a period when the NEB has been observed to sporadically expand into the NTrZ, we speculate that the NEB expansion conditions (and the resulting cyclogenesis) may be influencing the environmental conditions permitting the propagation of these waves.
2. The wave trains were initially restricted in longitude to packets $\sim 10^\circ$ wide, meaning that only ~ 7 – 10 wave crests were visible in the early detections. These packets appeared to the west of B1 and B2 and had lifetimes of a few months. The packets were latitudinally wider in the east than in the west, and the wave crests appeared to be sheared from southeast to northwest. Such a morphology is likely related to the changing wind across the NEB (centered on the westward NEBn jet at 17°N) and the visibly bright and 5- μm dark elongated rifts that could be seen in Figure 6 stretching across the NEB from southeast to northwest. The wave trains expanded to span $\sim 40^\circ$ – 50° longitude some 6–8 months after they were first detected and were most visible in 2017 March and April.
3. The waves were not visible when the NEB became chaotic. At 5 μm , the presence of a closely packed pattern of cyclones and anticyclones (typical of the end stages of an NEB expansion and contraction event) rendered the small-scale wave pattern invisible, although it could still be detected in visible light. However, strong rifting activity that is bright in the visible and dark at 5 μm (which was present from 90°W to 220°W in 2017 March) caused the wave pattern to be invisible at all wavelengths and potentially disrupted it completely. We suggest that relatively quiescent NEB conditions are therefore needed for the wave pattern to propagate.
4. The waves retained their 1.1 – 1.4 wavelength (a wavenumber of 260–330) at all epochs without notable increases or decreases with time. Simon et al. (2015) pointed out that this and the $\sim 2^\circ$ latitudinal extent of the waves are on the same scale as the atmospheric deformation radius (see Figure 8(f)), which may be playing a role in setting the length scale for these waves.

By analogy to waves associated with cyclones and anticyclones on Earth and in general circulation models, Simon et al. (2018) proposed both pure gravity waves (GWs; under the action of gravity and buoyancy forces) and/or inertio-gravity waves (IGWs; with wavelengths long enough to require consideration of the Coriolis term) as plausible explanations for the observed mesoscale wave pattern. In this analysis, we also consider short-wavelength Rossby waves (RWs), although we note that Jovian RWs typically have much longer wavelengths and a very different morphology than the mesoscale waves described here (e.g., NEB thermal waves with a 22° – 24° longitude wavelength were identified in the NEB in 2015–16; Fletcher et al. 2017b). We utilize Jupiter’s zonal-mean temperature structure retrieved from *Cassini* Composite Infrared Spectrometer (CIRS) data by Fletcher et al. (2016a) to explore the dispersion relationships of these three wave types. Although more recent Earth-based temperature observations are available, their analysis is ongoing, and the *Cassini* thermal structure from 2000 December can be used as a good qualitative proxy for present-day conditions within the NEB.

We take the dispersion relationship for linear GWs as (Holton & Alexander 2000; Sánchez-Lavega et al. 2011)

$$\omega^2 = (c_x - u)^2 k^2 = \frac{N^2 k^2}{k^2 + m^2 + 1/(4H^2)}. \quad (1)$$

Here ω is the intrinsic frequency; c_x is the longitudinal phase speed of the waves; u is the zonal wind determined from the thermal wind shear dT/dy (where y is the north–south distance); k and m are the zonal and vertical wavenumbers, respectively; N is the Brunt Väisälä frequency; and H is the scale height. Note that we take the meridional wavenumber to be zero, as the wave crests are nearly zonal, i.e., perpendicular to longitude and flow direction. The dispersion relationship for IGWs (e.g., accounting for the Coriolis parameter f) is given by (Section 4.6.3 of Andrews et al. 1987)

$$\omega^2 = (c_x - u)^2 k^2 = f^2 + \frac{N^2 k^2}{m^2 + 1/(4H^2)}. \quad (2)$$

Finally, the dispersion relationship for a quasi-geostrophic RW reduces to (Sánchez-Lavega et al. 2011)

$$c_x - u = -\frac{\beta_e}{k^2 + (f^2/N^2)(m^2 + (1/4H^2))}. \quad (3)$$

Here we have introduced the latitudinal gradient of the quasi-geostrophic potential vorticity ($\beta_e = dq_G/dy$, the “effective beta”; Andrews et al. 1987), evaluated following the method of Fletcher et al. (2016b). This is related to the change in the Coriolis parameter with latitude, which provides the restoring force for RWs.

Note that we consider only GWs, IGWs, and RWs, rather than Kelvin–Helmholtz instabilities, because the Richardson number ($N^2/(du/dz)^2$) is positive and much larger than one throughout the 80–800 mbar range sampled here. The dispersion relationships above rely on parameters that can be derived from the CIRS temperature measurements in the 0.1–0.8 bar range: zonal winds are estimated from the thermal wind equation (Andrews et al. 1987), and the buoyancy frequency utilized the measured and dry adiabatic lapse rates (using the local gravity and specific heat capacity). The mean zonal phase speed of the waves, c_x , is estimated to be

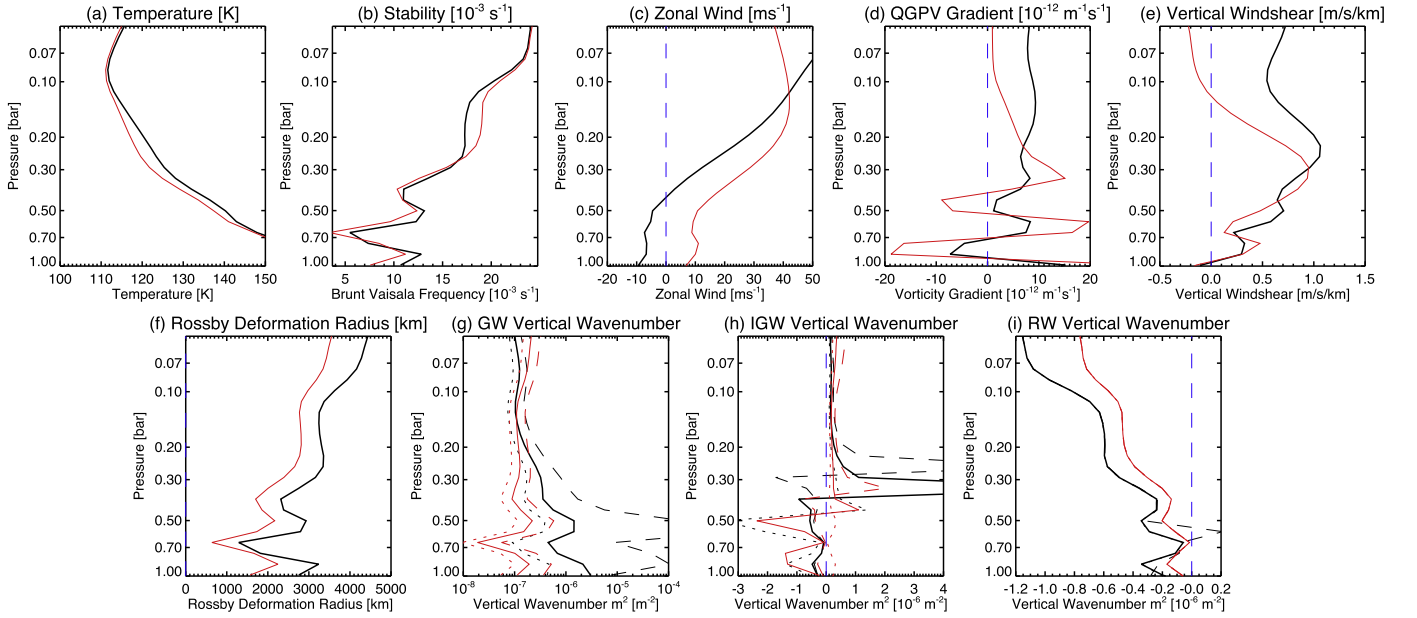


Figure 8. Exploring the properties of the NEB using *Cassini* CIRS temperature retrievals from 2000 (Fletcher et al. 2016a), comparing the latitudes of the NEB cyclones (16°N; solid black line) and NTrZ anticyclones (20°N; solid red line). We plot (a) the temperatures; (b) the Brunt Väisälä frequency; (c) the zonal winds estimated from the vertical wind shear in panel (e); (d) the latitudinal gradient of the quasi-geostrophic potential vorticity; (f) the Rossby deformation radius; and the square of the vertical wavenumber m in the case of pure gravity waves (g), inertio-gravity waves (h), and Rossby waves (i). The CIRS constrained temperatures between 80 and 800 mbar, so values outside of this range should be treated with caution. For the calculations of m^2 , we show estimates for $c_x = -5 \text{ m s}^{-1}$ (dashed line), $c_x = -15 \text{ m s}^{-1}$ (solid line), and $c_x = -25 \text{ m s}^{-1}$ (dotted line) for 16°N (black) and 20°N (red). Parameters based on first- and second-order derivatives of the $T(p)$ are highly uncertain, as described in the main text, and should be considered as a qualitative guide only. The blue dashed line indicates the zero point.

$-15.5 \pm 10 \text{ m s}^{-1}$ (from an average of the 2016–17 measurements of Simon et al. 2018), implying a slow westward motion with respect to the cloud-tracked zonal winds at 16°N ($u \sim -10 \text{ m s}^{-1}$ in the center of the NEB; Figure 8(c)). These dispersion relationships should strictly rely on constant N and u with altitude, which is not the case in Figure 8, and so should be considered only as approximations. These equations can be rearranged to estimate m to assess the likelihood of vertical propagation, first for GWs,

$$m^2 = \frac{N^2}{(c_x - u)^2} - k^2 - \frac{1}{4H^2}, \quad (4)$$

second for IGWs,

$$m^2 = \frac{N^2 k^2}{(c_x - u)^2 k^2 - f^2} - \frac{1}{4H^2}, \quad (5)$$

and finally for RWs,

$$m^2 = \frac{N^2}{f^2} \left(\frac{\beta_e}{u - c_x} - k^2 \right) - \frac{1}{4H^2}. \quad (6)$$

If $m^2 > 0$, then real solutions can be found, and vertical propagation of this wave type is permitted. If $m^2 < 0$, then the solutions are imaginary, and the wave could be trapped in the vertical at the level that it is observed.

Figure 8 shows these calculated quantities—temperatures, wind shears, Rossby deformation radius ($L_D = NH/f$), and m^2 —for the GW, IGW, and RW cases. These are provided at 16°N (the latitude of the cyclone chain in the NEB) and 20°N (the latitude of the associated anticyclones in the NTrZ). Before describing the results, we first caution the reader that the parameters in Figure 8 are subject to large uncertainties—wind shears and static stability both require derivatives of the retrieved temperatures with latitude and altitude, and estimates

of the winds (and associated vorticity gradients) require integration of these gradients with altitude. This can serve to magnify the 1–2 K uncertainties on the $T(p)$ profile in Figure 8(a), even if we consider the CIRS inversions to be “ideal” (Fletcher et al. 2016b). Additional errors arise from assumptions on vertical smoothing and variable information content with height, zonal averaging over Jupiter’s spatially variable temperatures (Fletcher et al. 2016a), and the altitude level of the cloud-tracked zonal winds. Quantifying the effects of these unknowns in a meaningful way is challenging, but the parameters in Figure 8 represent our best estimate from the CIRS data and are sufficient to show qualitative trends, rather than quantitative values.

With these caveats in mind, we explore the implications of the vertical wavenumbers in Figure 8. In the GW case, we find that vertical propagation is allowed at all altitudes sampled (m is always real in Figure 8(g)). The value of m varies considerably within the $c_x = -(15 \pm 10) \text{ m s}^{-1}$ uncertainly envelope quoted by Simon et al. (2018), but the central value of $m \sim 1 \times 10^{-3} \text{ m}^{-1}$ near 500–700 mbar is equivalent to a vertical wavelength of $\sim 6 \text{ km}$, or a third of a scale height. For IGWs in Figure 8(h), we find that $m^2 < 0$ for high pressures, but that vertical propagation is allowed for lower pressures. The transition between these regimes is sensitive to c_x , with more westward phase speeds ($c_x \approx -25 \text{ m s}^{-1}$) able to propagate vertically at deeper pressures ($p < 500 \text{ mbar}$), whereas slower phase speeds ($c_x \approx -5 \text{ m s}^{-1}$) could only propagate in the upper troposphere ($p < 300 \text{ mbar}$). Closer inspection of Equation (2) shows that IGW vertical propagation is inhibited when the intrinsic frequency ω is smaller than the Coriolis parameter f , which is the case for $p > 400 \text{ mbar}$ for waves with a $c_x = -15 \text{ m s}^{-1}$ phase speed. The IGWs are not conclusively ruled out for higher pressures ($p > 500 \text{ mbar}$), provided they form at the altitude at which they are observed, which is

estimated to be ~ 500 mbar from *Hubble* data (Simon et al. 2018). Finally, the vertical wavenumber for RWs is found to be negative almost everywhere—this is because $k^2 \gg \beta_e/(u - c_x)$ in Equation (6) for this short-period wave (so the value of c_x has negligible influence on m^2), with the second term only gaining prominence when $u \approx c_x$, which is the case for $c_x = -5 \text{ m s}^{-1}$ in Figure 8(i). Given that the mesoscale wave bears little resemblance to RWs previously identified on Jupiter and the fact that vertical propagation is prohibited, we deem this to be the least likely explanation for these waves. Given that both c_x and the background zonal u from the thermal wind equation are significantly uncertain, these estimates of m^2 should be considered as qualitative guides only.

Frustratingly, further progress on identifying the nature of this wave pattern cannot be extracted from these measurements alone. Preliminary GCM modeling (Simon et al. 2018) is similarly inconclusive. Both GWs and IGWs are plausible explanations, with the former propagating more easily in the vertical throughout the upper troposphere. It is reasonable to hypothesize that the $5\text{-}\mu\text{m}$ brightness and the *Hubble* reflectivity are being modulated by the same aerosol layers somewhere in the 400–800 mbar range. Finally, it has been previously noted that the latitudinal gradient of quasi-geostrophic potential vorticity ($\beta_e = dq_G/dy$, the “effective beta”; Andrews et al. 1987) changes sign across the NEB (Li et al. 2006; Rogers 2016). Figure 8(d) shows a complex vertical structure at 16°N – 21°N , with the gradient changing sign several times in the 400–1000 mbar range. Such sign changes are a necessary (but not sufficient) condition for baroclinic instability following the Charney–Stern criterion (Charney & Stern 1962). While not conclusive, it is at the very least suggestive of mesoscale GWs or IGWs related to instabilities in the upper tropospheric aerosol layers (400–800 mbar), modulating both the *Hubble* reflectivity and the $5\text{-}\mu\text{m}$ brightness.

5. Conclusions

Using a technique of “lucky imaging” to freeze atmospheric seeing, the VLT/VISIR and Gemini/NIRI instruments have provided the highest-resolution $5\text{-}\mu\text{m}$ views of Jupiter’s atmosphere obtained from Earth. Coupled with *Juno* JIRAM M-band maps from the first seven *Juno* perijoves (2016 August–2017 July) and *Hubble* and amateur imaging at visible wavelengths (Simon et al. 2018), this has enabled the detection of a mesoscale wave pattern in Jupiter’s NEB, often (but not always) associated with a chain of cyclones at 16°N (within the NEB) and associated anticyclones at 19°N – 20°N (in the NTrZ). The genesis and evolution of this wave pattern is unclear. The waves have a longitudinal wavelength of 1.1° – 1.4° (wavenumber 260–330, corresponding to a length of ~ 1300 – 1600 km) that does not change with time, the wave crests are aligned north–south with a slight northwestward tilt, they cause a 7–10 K brightness temperature modulation at $5\text{-}\mu\text{m}$ consistent with 10%–20% changes in the opacity of an upper tropospheric cloud, they exist over a limited $\sim 2^\circ$ latitude range near the northern edge of the NEB, and they start small (initially detected in longitudinal packets extending $\sim 10^\circ$ west of cyclones) but evolve to span a broad range of longitudes. The waves appear to be ephemeral, appearing and disappearing on timescales of weeks. They are removed or rendered invisible by

chaotic rifting activity within the NEB, which is present in 2017 March.

The true nature of the waves remain elusive. The thermal structure of the NEB was used to investigate GW, IGW, and RW dispersion relationships, finding that GWs are able to propagate vertically throughout the upper troposphere, whereas IGW propagation is only permitted at low pressures, and RW propagation is ruled out throughout this domain for a wave of this small scale. We cannot definitively rule out a wave source at higher pressures, where information on the thermal structure (and wave propagation conditions) is unavailable. But it is plausible that mesoscale waves (GWs or IGWs) could be modulating Jupiter’s upper tropospheric aerosols in the 400–800 mbar range. These aerosols are detected through their reflectivity (Simon et al. 2018) and their attenuation of $5\text{-}\mu\text{m}$ radiance originating from deeper atmospheric pressures. We note that this region of the NEB exhibits the necessary conditions to violate a range of instability criteria, favoring wave genesis at this latitude.

The linkage between these waves and the NEB cyclones is compelling but inconclusive, pending future numerical simulations. The presence of the waves today, compared to their rarity in previous years, could be related to the recent 2015–16 and 2016–17 expansion and contraction episodes of the NEB (Fletcher et al. 2017b), and we note that the waves were first spotted in association with two cyclones that had played a prominent role in the 2015–16 expansion. Changes to the tropospheric thermal conditions and their correlation with the presence of the mesoscale waves could provide insights into their genesis and will be the subject of future intensive study.

Fletcher was supported by a Royal Society Research Fellowship and European Research Council Consolidator Grant (under the European Union’s Horizon 2020 research and innovation program, grant agreement No 723890) at the University of Leicester. The UK authors acknowledge the support of the Science and Technology Facilities Council (STFC). Orton was supported by grants from NASA to the Jet Propulsion Laboratory, California Institute of Technology. A. Sanchez-Lavega and R. Hueso were supported by the Spanish projects AYA2015-65041-P (MINECO/FEDER, UE) and Grupos Gobierno Vasco IT-765-13. We are grateful to R. Morales-Juberias and R. Cosentino for discussions on the contents of this article. This investigation was based on thermal-infrared observations acquired at the ESO Very Large Telescope Paranal UT3/Melipal Observatory with program IDs 60.A-9620, 098.C-0681, and 099.C-0612. Observations were also obtained at the Gemini Observatory (program ID GN-2017A-Q-60), which is operated by the Association of Universities for Research in Astronomy, Inc., under a cooperative agreement with the NSF on behalf of the Gemini partnership: the National Science Foundation (United States), the National Research Council (Canada), CONICYT (Chile), Ministerio de Ciencia, Tecnología e Innovación Productiva (Argentina), and Ministério da Ciência, Tecnologia e Inovação (Brazil). The JIRAM project was founded by the Italian Space Agency (ASI), and we are grateful to all those who participated in the design of these data. The VLT observations are available through the ESO archive,¹¹ and the JIRAM observations are

¹¹ http://archive.eso.org/eso/eso_archive_main.html

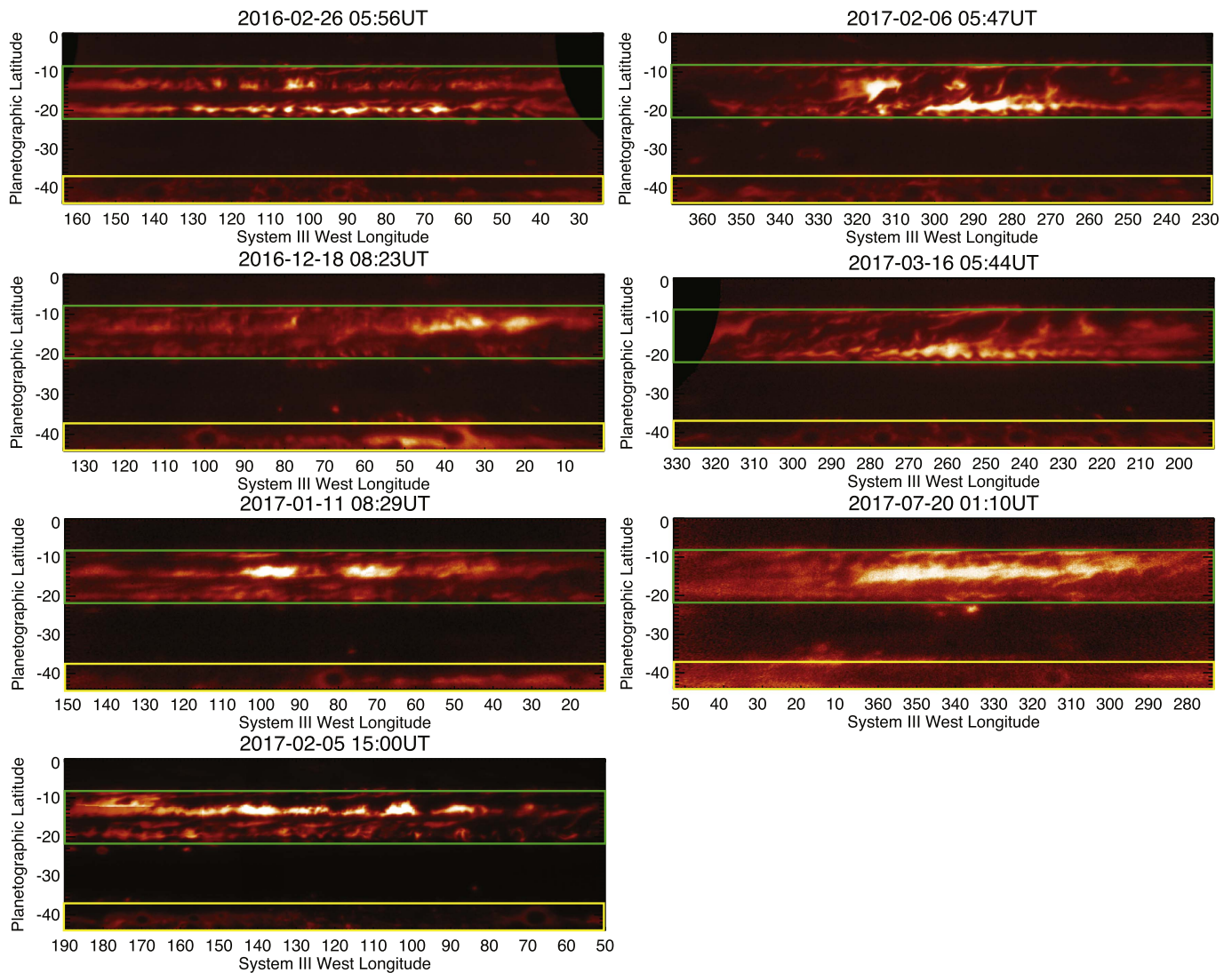


Figure 9. Maps of 5- μ m emission in the southern hemisphere, highlighting the SEB region in green and the SSTB region in yellow.

available through the Planetary Data System Atmospheres Node.¹² The lucky imaging made use of the Autostakkert software.¹³ The *HST* observations are associated with programs GO-14661 and GO-14756, with support provided to Simon, Wong, Barnett, and Orton by NASA through grants from the Space Telescope Science Institute (operated by the Association of Universities for Research in Astronomy, Inc., under NASA contract NAS 5-26555). The *HST* data can be obtained from the MAST archive.¹⁴

Facilities: VLT, *Hubble*, Gemini.

Appendix Status of Jupiter's Major Belts

To provide context for the changes observed in the NEB, we now describe additional insights available in the 5- μ m maps at other latitude bands.

¹² https://pds-atmospheres.nmsu.edu/data_and_services/atmospheres_data/JUNO/jiram.html

¹³ autostakkert.com


¹⁴ OPAL, <https://archive.stsci.edu/prepds/opal>, doi:10.17909/T9G593; WFCJ, <https://archive.stsci.edu/prepds/wfcj>, doi:10.17909/T94T1H

1. South Equatorial Belt (SEB).—Figure 9 reveals how the SEB emission had a banded appearance in early 2016, but this was significantly disrupted by an outbreak of convective plumes in early 2017. Although the SEB was not in a faded state (Fletcher et al. 2011), the mid-SEB outbreak produced 5- μ m dark clouds and bright peripheral lanes that extended between the prograde SEBn jet and the retrograde SEBs jet in a characteristic “S” shape reminiscent of the 2010–11 revival (Fletcher et al. 2017a). The outbreak occurred near 16°S, 300°W in late 2016 December and dominates the appearance of the SEB in 2017 February and March (region [4] of Figure 1).
2. South South Temperate Belt (SSTB).—A chain of anticyclonic vortices can be seen in the SSTB, appearing white in visible light and dark (i.e., cloudy) at 5 μ m. They are embedded in a belt of diffuse emission, and each displays peripheral rings associated with subsidence and aerosol clearing (e.g., de Pater et al. 2010). These large anticyclonic ovals dominate the temperate southern latitudes and are resolved in good detail by the VISIR burst-mode imaging (region [5] of Figure 1). Note that Oval BA does not exhibit any peripheral ring (it is located

near 320°W in 2017 February–March), suggesting that the cloud coverage of the southern temperate zones is too large to permit 5- μ m emission. A faint cyclonic region immediately west of Oval BA can be observed in emission near 33°S, 332°W in 2017 February.

3. North Temperate Belt (NTB).—Region [1] of Figures 1 and 3 indicates that plume activity on the southern edge of the NTB in 2016 October (Hueso et al. 2017; Sánchez-Lavega et al. 2017) corresponded to a change in the cloud opacity over the northern edge of the NTB. The 2016 February observations, before the NTB outbreak, indicated small and localized spots of emission, suggesting that much of the NTB was clouded over (i.e., faded). The 2017 observations all indicate a bright, broken band over the NTB(N). This sits northward of the deep red NTB(S) band that formed in the aftermath of the 2016 October outbreak and represents a clearing (revival) of the NTB(N).

ORCID iDs

Leigh N. Fletcher  <https://orcid.org/0000-0001-5834-9588>
 A. Adriani  <https://orcid.org/0000-0003-4998-8008>
 A. A. Simon  <https://orcid.org/0000-0003-4641-6186>
 M. H. Wong  <https://orcid.org/0000-0003-2804-5086>
 M. L. Moriconi  <https://orcid.org/0000-0003-2609-2620>
 F. Altieri  <https://orcid.org/0000-0002-6338-8300>
 G. Sindoni  <https://orcid.org/0000-0002-3348-7930>

References

- Adriani, A., Filacchione, G., Di Iorio, T., et al. 2017, *SSRv*, **213**, 393
 Andrews, D. G., Holton, J. R., & Leovy, C. B. 1987, *Middle Atmosphere Dynamics* (New York: Academic)
- Bjoraker, G. L., Wong, M. H., de Pater, I., & Ádámkovics, M. 2015, *ApJ*, **810**, 122
 Bolton, S. J., Adriani, A., Adumitroaie, V., et al. 2017, *Sci*, **356**, 821
 Charney, J. G., & Stern, M. E. 1962, *JAtS*, **19**, 159
 de Pater, I., Wong, M. H., Marcus, P., et al. 2010, *Icar*, **210**, 742
 Fletcher, L. N., Greathouse, T. K., Orton, G. S., et al. 2016a, *Icar*, **278**, 128
 Fletcher, L. N., Irwin, P. G. J., Achterberg, R. K., Orton, G. S., & Flasar, F. M. 2016b, *Icar*, **264**, 137
 Fletcher, L. N., Orton, G. S., Mousis, O., et al. 2010, *Icar*, **208**, 306
 Fletcher, L. N., Orton, G. S., Rogers, J. H., et al. 2011, *Icar*, **213**, 564
 Fletcher, L. N., Orton, G. S., Rogers, J. H., et al. 2017a, *Icar*, **286**, 94
 Fletcher, L. N., Orton, G. S., Sinclair, J. A., et al. 2017b, *GeoRL*, **44**, 7140
 Giles, R. S., Fletcher, L. N., & Irwin, P. G. J. 2015, *Icar*, **257**, 457
 Giles, R. S., Fletcher, L. N., & Irwin, P. G. J. 2017a, *Icar*, **289**, 254
 Giles, R. S., Fletcher, L. N., Irwin, P. G. J., Orton, G. S., & Sinclair, J. A. 2017b, *GeoRL*, **44**, 10
 Grassi, D., Adriani, A., Mura, A., et al. 2017, *GeoRL*, **44**, 4615
 Hodapp, K. W., Jensen, J. B., Irwin, E. M., et al. 2003, *PASP*, **115**, 1388
 Holton, J. R., & Alexander, M. J. 2000, *GMS*, **123**, 21
 Hueso, R., Sánchez-Lavega, A., Iñurriagarro, P., et al. 2017, *GeoRL*, **44**, 4669
 Irwin, P. G. J., & Dyudina, U. 2002, *Icar*, **156**, 52
 Irwin, P. G. J., Weir, A. L., Taylor, F. W., Calcutt, S. B., & Carlson, R. W. 2001, *Icar*, **149**, 397
 Kraaikamp, E. 2016, *S&T*, **132**, 68
 Lagage, P. O., Pel, J. W., Authier, M., et al. 2004, *Msngr*, **117**, 12
 Li, L., Ingersoll, A. P., Vasavada, A. R., et al. 2006, *Icar*, **185**, 416
 Nixon, C. A., Irwin, P. G. J., Calcutt, S. B., Taylor, F. W., & Carlson, R. W. 2001, *Icar*, **150**, 48
 Rogers, J. H., Fletcher, L. N., Adamoli, G., et al. 2016, *Icar*, **277**, 354
 Rogers, J. H. 2017, arXiv:1707.03343
 Sánchez-Lavega, A., del Río-Gaztelurrutia, T., Hueso, R., et al. 2011, *Natur*, **475**, 71
 Sánchez-Lavega, A., Rogers, J. H., Orton, G. S., et al. 2017, *GeoRL*, **44**, 4679
 Simon, A. A., Hueso, R., Inurriagarro, P., et al. 2018, *ApJ*, submitted
 Simon, A. A., Wong, M. H., & Orton, G. S. 2015, *ApJL*, **812**, 55
 Smith, B. A., Soderblom, L. A., Johnson, T. V., et al. 1979, *Sci*, **204**, 951
 Sromovsky, L. A., & Fry, P. M. 2010, *Icar*, **210**, 230
 Terrile, R. J., & Westphal, J. A. 1977, *Icar*, **30**, 274